Combustion and Flame 235 (2022) 111714

Contents lists available at ScienceDirect

Combustion and Flame

journal homepage: www.elsevier.com/locate/combustflame

Numerical study of flame spread in a narrow flow duct in microgravity – effects of flow confinement and radiation reflection

Yanjun Li, Ya-Ting T. Liao*

Case Western Research University, 10900 Euclid Avenue, Cleveland, Ohio 44106, United States

ARTICLE INFO

Article history:
Received 21 April 2021
Revised 21 August 2021
Accepted 21 August 2021
Available online 8 September 2021

Keywords:
Microgravity combustion
Concurrent-flow flame spread
Radiation reflection
Flow confinement

ABSTRACT

A three-dimensional numerical study is performed to investigate concurrent-flow flame spread over thin solid fuels in microgravity. The model considers the burning scenarios of a recently concluded ISS microgravity experiment, Confined Combustion. Cellulose based thin samples are burned in a small flow duct. The height of the flow duct and the radiation reflectance of the duct wall are varied. Flame development and steady spread flame characteristics are compared with the experimental results at various duct heights. The numerical results demonstrate that the confinement imposed by the duct walls accelerates the flow during the combustion thermal expansion, enhancing the conductive heat transfer to the solid samples. When the duct height is below a critical height, the flow confinement limits oxygen supply to the flame, and the duct wall acts as a conductive heat sink. As a result of the interplay of these effects, the flame spread rate and pyrolysis length first increase and then decrease as the duct height decreases. Eventually, the flame fails to spread at a quenching duct height. In addition, side-leading concave (two-teeth fork shaped) flames are observed below the critical duct height. This flame shape increases the flame surface area and facilitates oxygen transport to the combustion zone. When the duct wall reflectance varies, a higher reflectance yields a longer pyrolysis length and a faster spread rate. This is due to enhanced heat input to both the solid sample surface and the gaseous flame. This effect is most significant for medium duct heights. At large duct heights, the duct wall is far from the flame and the sample. At small duct heights, while flame spread rate increases with the wall reflectance, the pyrolysis and flame length remain similar as combustion is limited by oxygen supply.

© 2021 The Combustion Institute. Published by Elsevier Inc. All rights reserved.

1. Introduction

Fires in confined spaces can exhibit very different behaviors from fires in open spaces and can be more dangerous [1]. In 2019, 55% of fires in the US occurred in confined structures (e.g., residential buildings, vehicles) and accounted for 98% of the total property loss [1]. In many recent fire accidents of the high-rise buildings (e.g., Grenfell tower fire in 2017), confinement imposed by external structures on building façade was identified to contribute to the fast fire growth [2]. To address this concern, this work aims to study fire behaviors and flame spread in confined spaces. Specifically, the interactions between a spreading flame and its surrounding walls and effects of such interactions on flame characteristics (e.g., flame length, spread rate, flame shape) will be examined through numerical simulations.

Many past studies have focused on the mechanical (or aerodynamic) interactions between structures and fire, using stationary burners in rooms, corners, tunnels, or near walls [3,4,5]. Many other studies have focused on tunnel fires with ventilated flows [6,7]. In most of these studies, fires are simulated experimentally using stationary burners – the flame does not move. However, fires in most real scenarios involve flames that themselves move or spread across the fuel. Flame spread is one of the most important characteristics of a fire, as it determines the available time to control the fire or to escape the area.

Upward flame spread in open and confined spaces has been studied in many previous works [5, 8, 9]. It is commonly acknowledged to be an accelerating process – both the rate of fire spread and the length of the flame continually increase. From a safety point of view, this acceleratory nature is dangerous. It is generally unknown if upward-spreading flames would eventually approach a steady-state spread rate and a limiting length, because it is impractical to construct an experimental apparatus tall enough to address this problem. Buoyancy has a major influence on fire growth processes in normal gravity and may mask observation of the fundamental underlying physics. In addition, soot radiation, which increases with fire size, further complicates the problem.

* Corresponding author.
E-mail address: yating.liao@case.edu (Y.T. Liao).

https://doi.org/10.1016/j.combustflame.2021.111714
0010-2180/© 2021 The Combustion Institute. Published by Elsevier Inc. All rights reserved.

In a microgravity environment, buoyancy is essentially eliminated so that forced flow can be imposed on the sample independent of other parameters. Rather than being classified as upward (or in a particular direction), flame spread in microgravity is defined as concurrent-flow or opposed-flow depending on its direction relative to the flow. Note that on earth, upward flame spread is concurrent-flow as the flame spreads in the same direction as the buoyancy-driven flow.

For opposed-flow flame spread in confined spaces in microgravity, Nakamura et al. performed numerical simulations and compared flames from an open configuration and in a chamber enclosure [10]. Their results show that confinement increases not only the flame spread rate but also the combustion heat release rate. This is because the flow is accelerated in the enclosure, resulting in enhanced oxygen transport to the flame. Wang et al. performed opposed-flow flame spread microgravity experiments (using a drop tower) in flow tunnels with different heights [11]. They found that flame spread rate increases first and then decreases when the tunnel height decreases. They also performed numerical simulations and concluded this trend is due to the flow acceleration at different levels of confinement.

For concurrent-flow flame spread in microgravity, limiting flame lengths and steady spread rates were predicted by numerical models for thin and thick samples [12,13]. The steady spread and limiting flame length have been verified experimentally in space where thick plastic rods [14] and thin fabric samples [15] were burned in low-speed concurrent flows in a small duct aboard the International Space Station (ISS). In a recent NASA project (Saffire), a series of large-scale flame spread experiments were conducted in unmanned space vehicles [16,17]. The sample and flow duct in these experiments had a dimension of one order magnitude larger than prior experiments. Results yielded slower flame spread rates than seen in previous smaller-scale experiments for the same samples, even when all other environmental conditions were the same (oxygen, pressure, and flow speed). This demonstrates that the confinement can have a significant influence on the flame spread characteristics.

Several research groups conducted numerical studies to investigate similar situations [18,19,20,21,22]. For instance, Shih and T'ien used a steady two-dimensional model to study concurrent-flow flame spread over thin solids in a flow tunnel in microgravity. Their results showed that the flame spread rate increases as the tunnel height decreases [18], consistent with the previous experiments. However, when the tunnel height is very small, their results showed that conductive heat loss to the tunnel walls increases, slowing the spread rate. This eventually leads to flame quenching. Their results also showed that for the same tunnel height, the flame becomes longer, and the spread rate increases when the reflectivity of the tunnel wall increases. No steady state solution was achieved for wall reflectivity close to one. This may indicate that flame continues to grow when subjected to radiation reflection from the tunnel wall. Such a transient process cannot be captured by a steady state model.

A similar process was studied by Li et al. using a three-dimensional transient numerical model [21,22]. In their work, tunnel walls were simulated as black surfaces (no radiation reflection). Steady state was achieved in most of the simulated cases (except when the duct height is close to the quenching limit). The steady state flame spread rate first increases and then decreases when the tunnel height decreases. When the tunnel height was reduced to near the quenching height, the transient model of Li et al. captured an oscillating flame: flame length, reaction intensity, and maximum flame temperature oscillated with time before the flame quenched.

Shih [19] and Malhotra et al. [20] simulated respectively concurrent [19] and opposed [20] flow flame spreads over parallel thin solid fuel sheets in microgravity using steady two-dimensional models. The fuel sheets were oriented parallel to the flow direction. The flow confined between adjacent sheets is similar to flow in a tunnel. At first, as the fuel sheets are brought together, the spread rate increases as the separation distance decreases. For intermediate fuel-sheet-separation distances, steady solutions were not obtained unless there was no radiation interaction between the flame and the fuel. When the separation distance is further decreased, the flame spread rate decreases and eventually the flame quenches due to flow resistance, limited thermal expansion, and oxygen starvation.

These numerical studies suggest that flow confinement and radiation reflection play important roles on the burning behaviors of solid combustibles (steady, continuously growing, or quenching). They also affect the characteristics of flame spread (flame length and spread rate). To further elaborate the effects of confinement on flame spread, Li et al. conducted microgravity experiments aboard the International Space Station (ISS) [23]. In their project, Confined Combustion, thin cotton-blend fabrics were burned in concurrent flows in a flow duct. The flow was imposed by an electric fan upstream to the duct inlet. Flow was measured by an air velocity transducer positioned in the fan section between the flow straightener and the duct inlet screen. To create different levels of confinement, two flow baffles were placed parallel next to the sample, one on each side symmetrically. Different levels of radiation reflection were imposed by using three different types of baffles, black anodized and polished aluminum and transparent polycarbonate baffles. Flow speeds and sample-baffle distances were also varied. At high flow speeds ($>$ 15 cm/s), Li et al. observed an accelerating flame: flame length and flame spread rate continuously grew throughout the test. When the flow speed was reduced (e.g., 6 cm/s), the flame reached a steady state with a constant spread rate. The steady flame spread rate increases first and then decreases when the baffle distance decreases. When comparing between the three different types of baffles, the flame spread rate was highest for the polished baffles and lowest for the transparent baffles.

Confined Combustion was the first to examine the combined effects of flow confinement and radiation reflection on concurrent-flow flame spread in microgravity. While qualitative discussions were given, it was challenging to discuss such effects quantitatively. As in many other microgravity experiments, the number of test points and diagnostics are limited. In addition, the spectral radiation properties of the baffles were hard to control, adding complexity when interpreting the results.

The objective of this work is to further investigate the interplay of the flow confinement and radiation reflection and their combined effects on flame characteristics. This is achieved through a three-dimensional transient numerical study. The geometry and burning scenarios are based on the Confined Combustion experiments [23]. The height of the flow duct and the radiation reflectance are systematically varied. The detailed profiles of the gas and solid phases, including the gas temperature, reaction contour, and heat fluxes on the sample surface, are compared between different cases. The results are also compared with the microgravity experiment data.

2. Numerical model description

The numerical model used in this work is based on a three-dimensional transient Computational Fluid Dynamic (CFD) in-house program. This model has been proven robust and validated against experimental data in a wide range of oxygen and flow conditions [15,16].

The model simulates the gaseous flame and the solid fuel sample. In the gas phase, the combustion and transport processes are

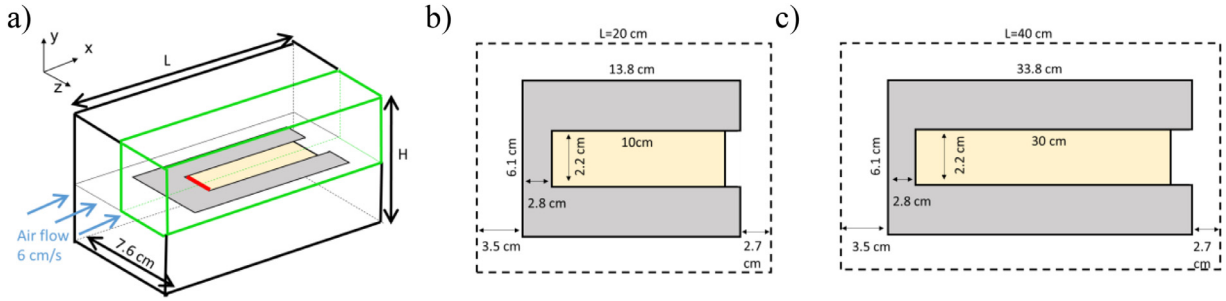

Fig. 1. Model configuration (not to scale). a) Sample, sample holder, and the flow duct. b) Sample dimensions used in the model validation. c) Sample dimensions used in parametric studies on duct height and duct ceiling radiation reflection.

simulated using direct numerical simulation. Three-dimensional transient Navier-Stokes equations are solved for the conservation of mass, momentum, energy, and species. One-step, second-order, finite rate global Arrhenius kinetics is assumed for the gas-phase reaction. Radiation Transfer Equation is also solved for gas radiation. In the solid phase, the mass and energy conservation equations are solved for the fuel sample and the sample holder. A two-step in-depth pyrolysis model is applied for the thermal decomposition of the sample fuel [15]. Gray diffusive surface radiation is considered on the surface of the sample and sample holder. The gas and solid phases are coupled to each other through interfacial boundary conditions. More detailed model descriptions, including theoretical formulation, gas and solid properties, mesh arrangement, time marching schemes, and numerical parameters can be found in previous papers [15,24,25].

The model configuration in this work is shown in Fig. 1. A thin solid sample (a cotton-blend, consisting of 75% cotton and 25% non-combustible fiberglass) is mounted on a sample holder and is positioned in the center of a flow duct. A uniform air flow of 6 cm/s is imposed at the duct inlet. Ignition of the sample is achieved by applying an external heat flux on the upstream leading edge of the sample. The applied heat flux follows a Gaussian distribution with a peak value of 2.39 W/cm^2 occurring 0.3 cm away from the sample leading edge. 98% of the ignition energy ($\sim$ 1.39 W) is distributed within 0.6 cm from the sample leading edge. After ignition (defined when the maximum gas temperature exceeds 1500 K), the external heat flux is reduced to zero at a constant rate in 3 s. The simulation conditions are in zero gravity, with ambient pressure of 1 atm and ambient temperature of 300 K.

The model configuration and the sample selection are based on the ISS project, Confined Combustion [23]. Dimensions corresponding to the experiments are first simulated (Fig. 1b). This allows direct comparisons between the modeling and experimental results (discussed in Section 3). After the model is validated against the experimental data, parametric studies are performed against flow duct height and the duct ceiling reflectance. In the parametric studies (discussed in Section 4), the height of the flow duct (H) varies between 1.5 cm and 15.0 cm. Longer lengths of the flow duct and fuel sample are used compared to the experiments (dimensions listed in Fig. 1c). This is to allow sufficient time (and distance) for the flame development and to facilitate the observation of the steady spreading flame.

In all simulations, symmetry boundary conditions are applied on the plane along the sample center line ($z = 0$, referred to as the center plane hereafter) and on the half sample thickness plane. This reduces the computational domain to a quarter (marked by the green box in Fig. 1a).

A constant temperature of 300 K is assumed on all duct walls. The duct ceiling ($y = H/2$, the wall parallel to the sample) is assumed to be gray diffusive (radiation heat transfer is independent of wavelength and directions). The radiative reflectance (ρ) of the duct ceiling varies between 0 (black surface) and 1.0 (fully-reflecting surface). The duct side wall ($z = 3.8$ cm, the wall perpendicular to the sample surface) is assumed to be a black surface.

All simulations are performed on the Case High Performance Computing Cluster at Case Western Reserve University. The total mesh ranges from 476k – 810k and the simulations typically require $\sim$ 120 to 226 h with parallel computing using 12 processors.

3. Validation against microgravity experiments

3.1. Transient flame growth process

In all simulated cases, the flame grows initially after ignition and then reaches a limiting length and a steady spreading rate. This is consistent with the observations in the microgravity experiment: the flame reaches a steady state at low flow speeds. The transient flame development process is demonstrated using a representative case ($H = 5$ cm, $\rho = 0$) in Fig. 2 (right panes). The modeling results are compared to a test of the ISS experiment. In the test, the sample was positioned between in a pair of black baffles with inter-baffle distance of 5 cm. Imposed flow speed was 6 cm/s. Flame images from the experiments are shown in Fig. 2 (left panes).

A reaction kernel was observed almost immediately after the ignitor was energized (time = 1 s in Fig. 2). Shortly after ignition (t $\sim$ 10 s), the flame reached steady state and spread downstream along the sample surface. Numerical and experiment results show similar flame shapes during the steady flame spread and the flame standoff distance (distance from the flame to the sample surface) increases in the downstream direction. When the flame tip reached the end of sample (t $\sim$ 50 s), it rounded to the sample surface. This was caused by the absence of no-slip boundary condition downstream of the sample (Fig. 1b). Eventually, the flame consumed all the combustibles and quenched. Fig. 2 demonstrates that the numerical model captures the transient flame growth and spread progresses observed in the experiment.

In Fig. 2, the high temperature region (e.g., $T > 1200$ K) in the simulation (right panes) is twice as long as the visible flame in the experiment images (left panes). Note that, in a concurrent flow, heat of combustion is transported downstream to the reaction zone via diffusion and convection. In this figure, flame profile (black lines in the right panes) is defined using fuel gas reaction rate at 10^{-3} g/cm^3/s. It shows that this definition of flame region matches well with the visually observed flames in the experiments.

Flame positions versus time in both numerical and experiment results are plotted in Fig. 3. In experiments, the flame profiles are extracted through image analysis using a custom MATLAB code [23]. The flame images are first transformed into gray scale to obtain the flame luminance information. The gray-scale images are

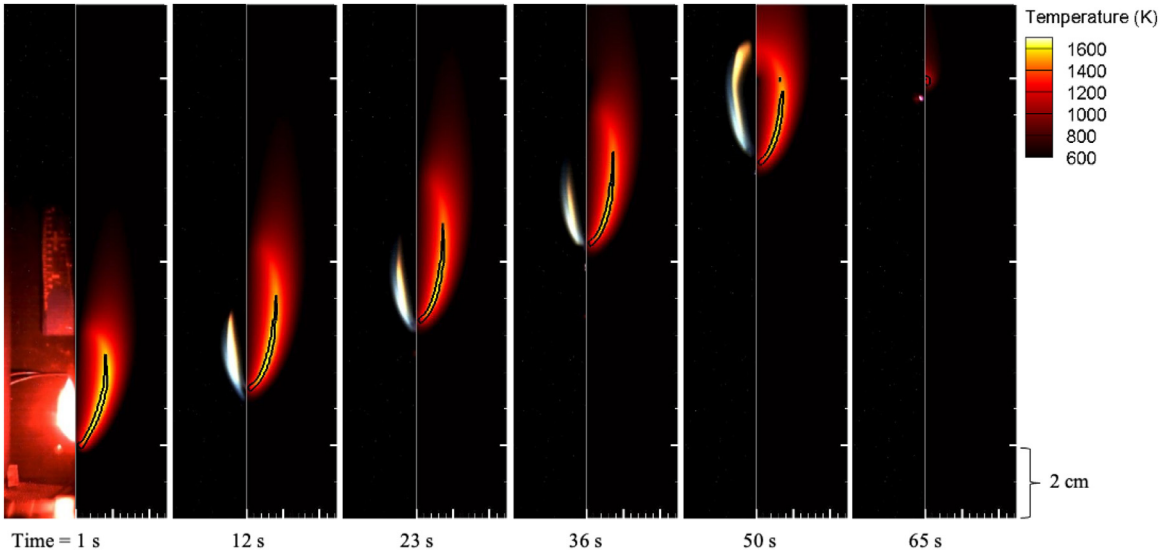

Fig. 2. Comparison of the flame growth between microgravity experiment (left panes) and numerical simulation (right panes). The black lines in the numerical simulation (right panes) are the isolines of fuel vapor reaction rate of 10^{-3} g/cm^3/s. $H = 5$ cm, $\rho = 0$.

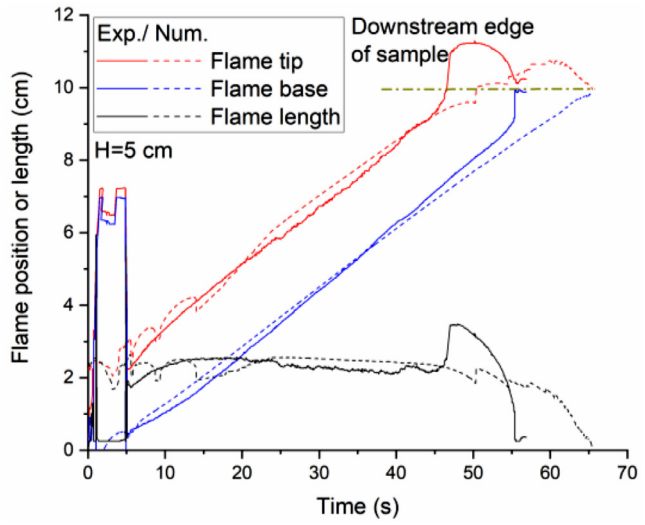

Fig. 3. Flame locations and flame length versus time. $H = 5$ cm, $\rho = 0$.

then transformed into black and white binary. The flame tip, flame base, and flame length are determined using this binary flame profile. Fig. 3 shows that the model quantitatively captured the flame growth and the steady spreading state.

Notice that in the experiment results, the flame tip exhibits a sudden advancement when reaching the downstream end of the sample (t $\sim$ 45 s). This is because in the experiment, flow confinement was imposed by two parallel baffles. The baffles have the same dimensions of the sample holder and extend only 1 cm downstream to the sample trailing edge (Fig. 1b). When the flame tip is near the end of the sample and is close to the baffle trailing edge, oxygen can diffuse upstream into the inter-baffle region. Fuel vapor can also transport beyond and burn outside of the baffle region. These do not occur in the numerical simulations where the confinement is directly imposed by flow duct walls.

3.2. Flame spread rate and flame length at steady state

Steady state flame lengths and spread rates at different duct heights from experiments and from numerical modeling are compared in Fig. 4. The flame spread rates are deduced by applying linear regression to the flame positions when the flame spread over the center portion of the solid fuel (4 - 7 cm). The average flame length is also deduced in the same time period. Note that the deduced flame length is associated with the definition of the flame region. However, the steady-state flame spread rate is independent of flame definitions.

The numerical results are consistent with the experimental observation: the flame spread rate and flame length increase first and then decrease when the duct height decreases. This non-monotonic trend was discussed previously by Li et al. [21,22]. Three major effects of confinement were identified. The first effect is enhancement of conductive and convective heat transfer to the sample surface. This is through forcing the flame to stay close to the sample surface (at very small duct heights) and flow acceleration due to thermal expansion of the combustion gasses. This effect increases the solid burning rate and intensifies the gas phase reaction as the duct height decreases. The second and third effects are the reduction of oxygen supply to the flame zone and introduction of heat loss to duct walls. These weaken the flame and eventually lead to a quenching duct height below which the flame fails to spread. Note that in the experiment, at $H = 1$ cm, the flame did not spread downstream and quenched immediately after the ignitor was off. The quenching duct height occurs between $H = 1$ and 2 cm. Note that this quenching duct height may depend on many factors including fuel type, flow speed, ambient oxygen percentage, and thermal boundary condition (300 K in the work) and radiation properties of the duct wall. At large duct heights, the difference of the flame spread rate between simulation and experiment is minimal (e.g., 3.7% difference for $H = 7.6$ cm). However, the difference is larger at smaller duct heights. This once again is suspected to be due to different hardware setups. In the experiments, the hardware flow characterization tests showed that flow in the inter-baffle region is lower than the imposed flow speed when the inter-baffle distance is small [23]. Friction on the sample surface and flow resistance diverted the flow to the extra-baffle region. This resulted in lower flame spread rate and flame length compared to the numerical predictions. Also note that while the spread rate is independent on the flame definitions, the flame length can vary when different thresholds are selected. Nevertheless, the model was able to replicate the experimentally observed influences of confinement on the flame characteristics.

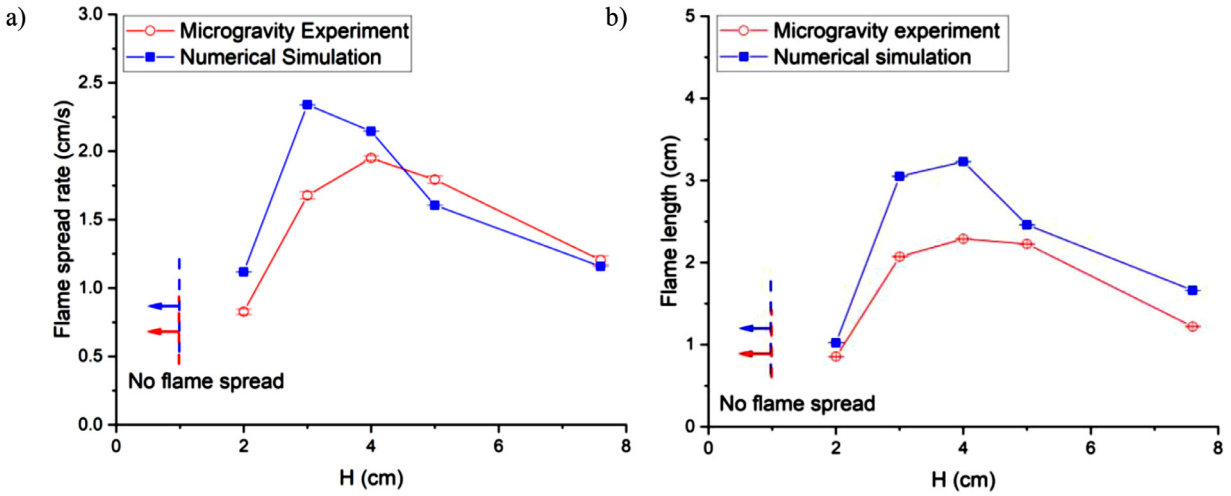

Fig. 4. Flame lengths and spread rates at the steady state at different duct heights. Results are for $\rho = 0$ (black baffles in the ISS experiments) and imposed flow speed of 6 cm/s. The error bars denote the 95% confidence internals of the measurements.

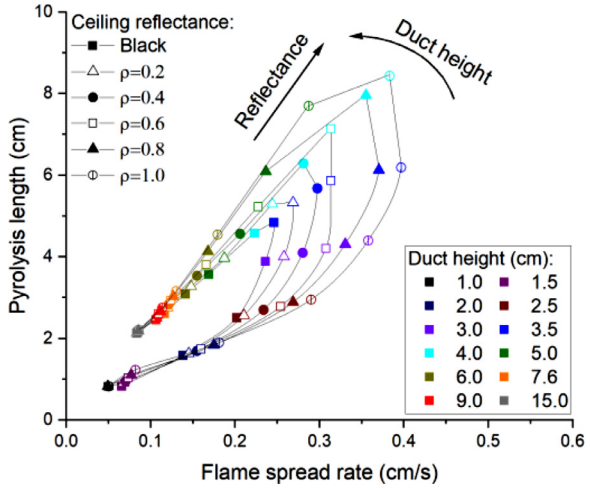

Fig. 5. Steady state flame spread rate and pyrolysis length at different duct heights and radiative reflectance. Duct height increases in the counter-clockwise direction around the black isoreflectance lines. Duct ceiling reflectance increases from the inter-most to the outer-most isoreflectance lines.

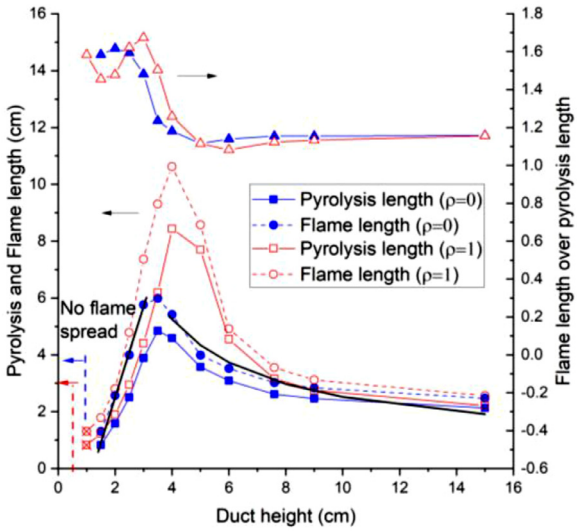

Fig. 6. Flame and pyrolysis lengths at steady spreading state at different duct heights. The cross symbols denote partial flame spread. The pyrolysis zone is defined as the region where solid mass burning rate exceeds 10^{-5} g/cm^2/s and the flame region is defined using fuel gas reaction rate $> 10^{-4}$ g/cm^3/s. Black lines denote fittings of the flame length at $\rho = 0$. Left fitting equation: $\boldsymbol{L_f} = 3.2\boldsymbol{H} - 3.9$, right fitting equation: $\boldsymbol{L_f} = 18.2/\boldsymbol{H} + 0.7$.

4. Parametric studies on duct height and radiation reflection

4.1. Flame spread rate, flame length, and pyrolysis length

To investigate the combined effects of the duct height and the radiation reflection, pyrolysis length and flame spread rate from all simulated cases are compared in Fig. 5. Here, the pyrolysis zone is defined as the region where solid mass burning rate exceeds 10^{-5} g/cm^2/s [24]. When ceiling reflectance (ρ) is fixed (see black isoreflectance lines), both flame spread rate and pyrolysis length increase and then decrease when the duct height increases (counter-clockwise direction around the loops). This remains true for all duct reflectance. At a fixed duct height (symbols of the same colors in Fig. 5), both pyrolysis length and spread rate increase when ρ increases. While this phenomenon is generally true for all duct heights, it is most prominent at medium simulated duct height $H = 4$ cm (maximum distance observed between the black isoreflectance lines), consistent with the findings in Confined Combustion [23]. Below this duct height, the dependence of the pyrolysis length on the ceiling reflectance is less significant than that of flame spread rate (for example, at $H = 3$ cm, when ρ increases from 0 to 1, pyrolysis length increases by 13% and the flame spread rate increases by 52%). At the smallest and largest duct heights ($H = 1.5$ and 15 cm), the pyrolysis length and spread rate remain similar when ρ varies. At $H = 1.0$ cm, at large reflectance ($\rho > 0.4$), flame spreads downstream and consumes the upstream $\sim$ 10 cm portion of the solid (partial flame spread) before extinction whereas no sustained flame is observed at small reflectance ($\rho \leq 0.4$).

Notice that in Fig. 5, at any fixed duct height, the pyrolysis length is linearly proportional to the spread rate. This phenomenon is also observed in previous experiments for concurrent flow flame spread under different flow speeds and oxygen concentrations [16,26,15,27,28].

In Fig. 6, the flame and pyrolysis lengths at different flow duct heights for black ($\rho = 0$) and reflecting ($\rho = 1$) ceilings are compared. Compared to the black ceiling, flame fails to spread at a lower duct height for the reflecting ceiling (1.5 cm vs. 1 cm). Also

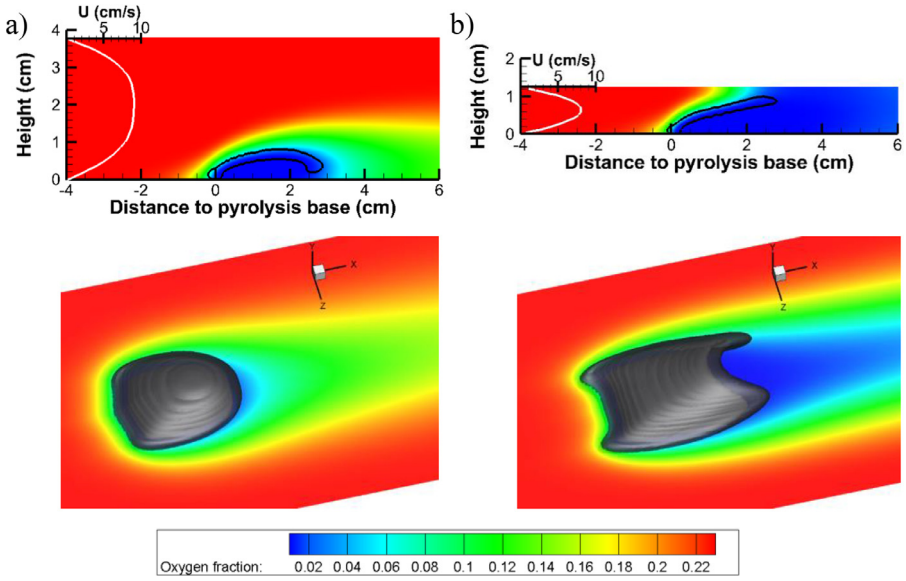

Fig. 7. Effects of confinement on flame shapes. Top: Upstream flow profile (white line), mass fraction of oxygen (color contour), and flame shape (black line) on center symmetric plane. Bottom: three-dimensional isosurface for fuel vapor reaction rate and mass fraction of oxygen near the sample surface ($y = 0.2$ cm). (a) $H = 7.6$ cm, $\rho = 0$. (b) $H = 2.5$ cm, $\rho = 0$.

notice that in Fig. 6, the optimal duct height (where the maximum flame/pyrolysis lengths occur) is larger for the reflecting duct ceiling than the black ceiling ($H = 4.0$ and 3.5 cm respectively). Above the optimal duct height, the flame and pyrolysis lengths both increase when duct height decreases and the flame-pyrolysis length ratio remains at1.15–1.2. Below the optimal duct height, flame and pyrolysis lengths both decrease with decreasing duct height and the flame- pyrolysis length ratio increases (except near the quenching duct height). These behaviors will be discussed below.

Note that below the optimal duct height, the combustion is under-ventilated and is controlled by the oxygen supply to the confined space, $\dot{m}_{O_2} \sim \rho_{air} UHWY_{O_2}$. Here, U is ambient flow velocity, W is the duct width, and ρ_{air} and Y_{O_2} are the density and mass fraction of oxygen of the ambient air respectively. The flame and pyrolysis lengths are observed to be linear to the duct height at both ceiling reflectance (see black line in Fig. 6). Above the optimal height, flow acceleration during combustion thermal expansion plays a crucial role on the flame spread. Assuming the volumetric expansion of the hot reacting gas mixture is approximately the same, the flow acceleration is expected to be inversely proportional to the duct cross-sectional area (WH). As a result, the flame spread rate and flame length are expected to be proportional to 1/H.

4.2. Flame shape

The flame profiles for two duct heights are compared in Fig. 7. For large duct heights ($H = 7.6$ cm or H/2 = 3.8 cm), the flame is far from the ceiling. The maximum flame standoff distance is $\sim$ 1 cm. The side-view flame profile (Fig. 7a, Top) resembles the flow boundary layer on the sample surface, except near the downstream flame tip. It is similar to that reported in previous work [26,28]. For a diffusion flame spreading over a solid combustible, the fuel vapor generated on the sample surface needs to diffuse across the viscous flow boundary layer to meet the oxidizer. Near the downstream flame tip region, for a narrow sample, oxygen is able to transport (via convection and diffusion) to the sample surface from the two sides (see Fig. 7a, Bottom). Hence combustion occurs near the sample surface (flame standoff distance decreases slightly near the downstream flame tip). The three-dimensional (3D) isosurface of the reaction contour (Fig. 7a Bottom) shows that the flame has a centerline-leading profile at the downstream front region (i.e., the center part of the flame travels ahead of the two sides of the flame). This centerline-leading flame shape was also reported in previous work [15,28,29] and was attributed to the flame heat loss to the side sample holders.

When the duct height is reduced to $\sim$ 3 cm (H/2 = 1.5 cm, close to the flame standoff distance), the flame extends to the ceiling resulting in a blockage of oxygen to the downstream region (Fig. 7b). This duct height is slightly below the optimal duct height where the flame length has a maximum value (Fig. 6). This oxygen blockage has a profound influence on the flame shape. The 3D flame profile (Fig. 7b Bottom) shows that the flame has a reversed shape at the downstream flame front. Due to the limited oxygen supply downstream of the flame front, the combustion near the sample centerline is incomplete. The unburned gas fuel needs to diffuse to the sides, seeking fresh air flow. Compared with the conventional flame shaped observed for larger duct height (Fig. 7a), this side-leading concave (two-teeth fork shaped) flame front increases the flame-pyrolysis length ratio (Fig. 6). Furthermore, this concave flame shape yields a larger surface-volume ratio of the flames, facilitating oxygen diffusion into the reaction zone. This mechanism resembles that for the near quenching finger flames [30,31]. Also notice that at this small duct height, the flame base on the centerline is more downstream compared with the flame at the larger duct height. While the flow supplies oxygen to the upstream flame base through convection, the duct ceiling limits oxygen diffusion to the combustion zone from the top at the small duct height. Similar to the flame front, the combustible vapor in the centerline region at the flame base needs to flow further downstream to react with the oxygen from the lateral sides.

The flow profile also contributes to the different observed flame shapes. The flow velocity profile along the duct height is plotted in Fig. 7 (white lines in the top plots). When the flame spreads to the center potion of the solid fuel, the flow is fully developed into a parabolic profile [32]. Due to the boundary layer developed on both the sample surface and duct ceiling, the flow accelerates in the mid plane (the maximum flow speed is $\sim$ 9 cm/s). Notice that when the duct height reduces to 2.5 cm (Fig. 7b), the flame tip enters the boundary layer of the duct ceiling where it experiences

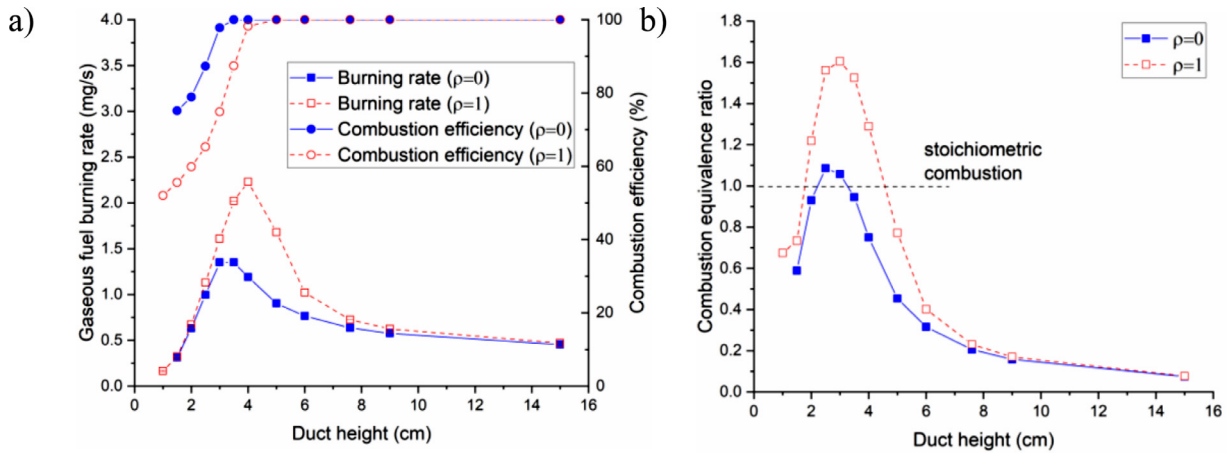

Fig. 8. Fuel vapor burning rate and calculated combustion efficiency at different duct heights. The combustion burning rate with reflection is always higher than without reflection.

a large velocity gradient. The momentum loss due to viscosity contributes to the reduction of the flame length at the small duct height. This may also contribute to the insensitive dependency of flame length on the reflectance (Fig. 5) at small duct heights.

4.3. Combustion efficiency and equivalence ratio

Fig. 8a demonstrates the influences of the flow confinement on the total fuel vapor reaction rate and the combustion efficiency (fuel vapor reaction rate over solid fuel mass burning rate). At large duct heights, the combustion efficiency is 100% and the gas reaction rate increases when the duct height decreases. This is because of the aforementioned enhancement of the conductive and convective heat transfer to the sample surface and the resulting increased solid burning rate as the duct height reduces. Note that the heat transfer due to the temperature gradient on the sample surface and due to flow convection are combined and will be referred to as conduction in the following text.

When the duct height is reduced to the optimal duct height (4 cm for $\rho = 1$ and 3.5 cm for $\rho = 0$), the combustion efficiency drops below unity due to oxygen depletion. The incomplete combustion and increased heat loss to the duct ceiling both reduce the flame temperature and gas burning rate as the duct height approaches the quenching height. Compared to the black ceiling, the reflective ceiling is expected to result in a higher solid burning rate (due to enhanced heat feedback to the solid surface). This higher solid burning rate requires a higher oxygen flow rate for complete combustion. Consequently, the combustion efficiency drops below unity at a higher duct height for the reflective ceiling compared with the black ceiling.

Also note that, the reflecting ceiling has a larger gas reaction rate. This is most obvious at middle duct heights. At a large duct height, the sample and the flame are distant from the duct ceiling. At small duct heights, combustion is limited by the oxygen supply (ventilation-controlled). In these limiting cases, gas combustion is less sensitive to ceiling reflection.

The steady state combustion equivalence ratio is also calculated as follows.

$$\phi = \frac{\left(\dot{m}_{fuel}/\dot{m}_{O_2}\right)_{avail}}{\left(\dot{m}_{fuel}/\dot{m}_{O_2}\right)_{stoi}} = \frac{r\tau\rho_s v_f}{\rho_{air} U H Y_{O_2}}$$

Here, r is the stochiometric oxygen-fuel mass ratio. ρ_s, τ, and W_s are the density, thickness, and width of the fuel samples respectively. The calculated equivalence ratio is plotted on Fig. 8b. When the duct height is above the optimal duct height, ϕ increases when the duct height decreases. At the optimal duct height, the combustion equivalence ratio exceeds unity. This is observed at both ceiling reflectance. This further suggests that the controlling mechanism of the optimal height is the oxygen starvation.

4.4. Heat flux on the sample surface

To understand the effects of the duct reflectance, the gas and solid profiles are compared between black and reflecting ceilings. For large duct heights (e.g., $H = 7.6$ cm, Figs. 9a and 9b), the ceiling is relatively far from the sample. For both black and reflecting ceilings, the conductive heat flux from the flame dominates the pyrolysis region. For small duct heights (e.g., $H = 2.5$ cm, Figs. 9c and 9d), the upstream flame base stays closer to the sample surface and the temperature of the flame is noticeably higher than for large duct heights. As a consequence, the conductive heat flux for small duct heights is higher than that of the large duct heights. This is true for both ceiling types. For the black ceiling, the duct height does not have a significant influence on the radiative heat input to the sample. For the reflecting ceiling, the radiative heat flux becomes comparable to the conductive heat flux at a small duct height.

The gas profile also shows an overall higher flame temperature for the reflecting ceiling compared to the black ceiling. This is more obvious at small duct heights (Figs. 9c and 9d). In this simulation, the combustion products (CO_2 and H_2O) participate in radiative transfer by emitting and absorbing radiation. It is suspected that the higher heat flux from the reflecting ceiling also transfers more heat to the reacting gas mixture and promotes combustion.

Also notice that, at the small duct heights, while the flame exhibits a side-leading concave front as shown in Fig. 7b, the pyrolysis front remains relatively flat across the sample width (Fig. 9c). On the sample surface profile shown in Figs. 9c and 9d, the pyrolysis front is slightly longer than the flame length on the center plane. However, the side-leading concave flame shape prolongs the overall flame length. This explains the increasing flame-pyrolysis length ratio with decreasing duct height in Fig. 6. It also leads to a larger preheat region and enhanced heat input to the solid surface.

Average conductive and radiative heat fluxes (area average) in the pyrolysis region for different cases are quantitatively compared in Fig. 10. For a black ceiling (solid symbols) for all duct heights, the conductive heat flux is greater than the radiative heat flux from the flame and it dominates the solid pyrolysis process. When the duct height decreases, the conductive heat flux remains constant for large duct heights. When the half duct height decreases to close to the flame height, the flame is pushed towards the sample hence

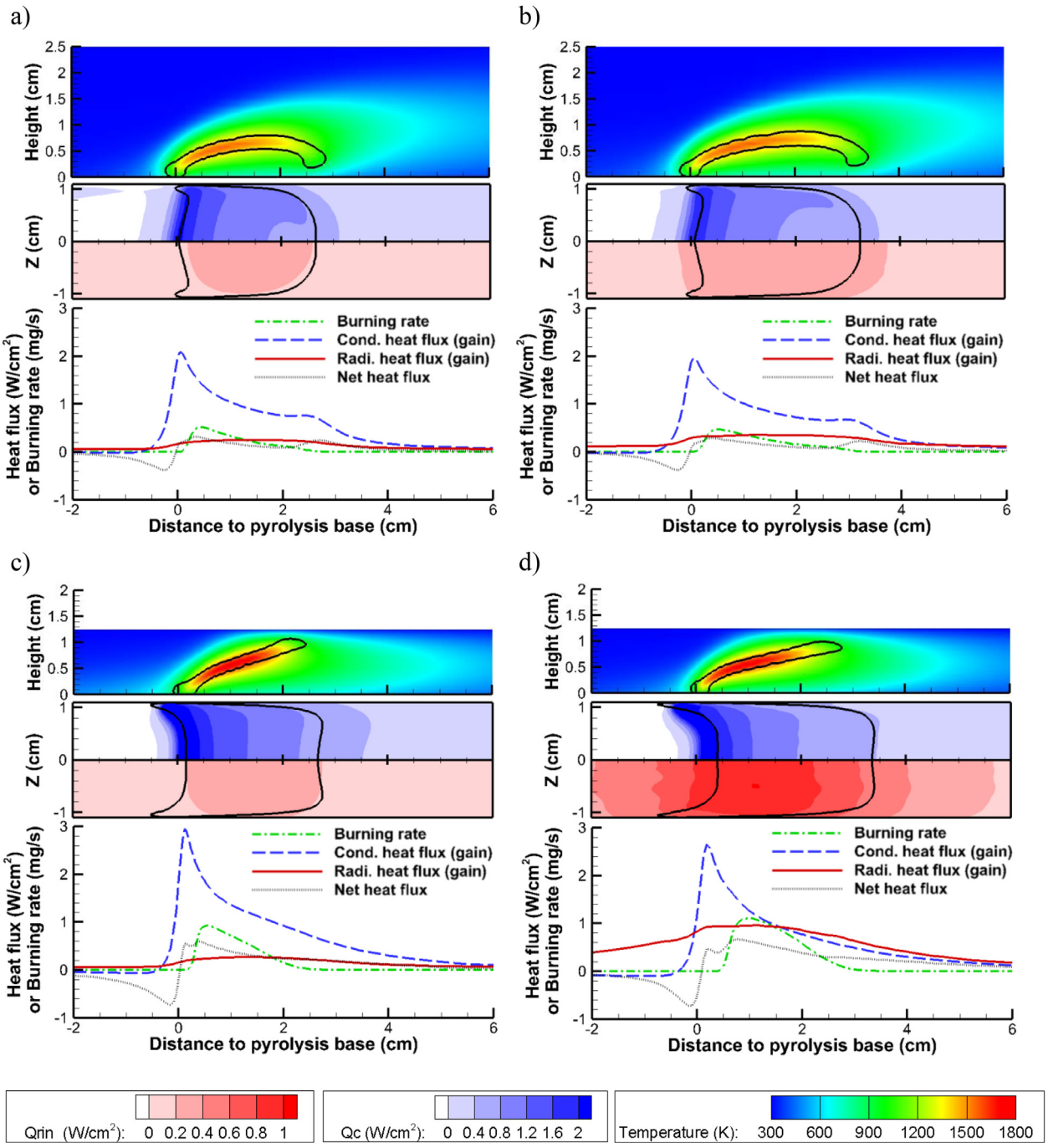

Fig. 9. Gas and solid profiles. Top: flame shape (black line) and gas temperature on the center plane. Middle: conductive (blue) and radiative (red) heat flux on the sample surface. Blackline denotes the pyrolysis zone. Bottom: Heat flux distribution along the sample centerline. (a) $\rho = 0$, $H = 7.6$ cm. (b) $\rho = 1$, $H = 7.6$ cm. (c) $\rho = 0$, $H = 2.5$ cm. (d) $\rho = 1$, $H = 2.5$ cm. (For interpretation of the references to color in this figure legend, the reader is referred to the web version of this article.)

the conductive flux increases. This somewhat compressed flame also increases the flame radiative heat flux when the duct height decreases. However, when the height reduces below 3 cm, combustion is incomplete (Fig. 8) and the radiative heat flux decreases due to the reduced flame temperature (compared with that at the optimal duct height of 3.5 cm).

For the reflective ceiling (open symbols, Fig. 10), the radiative flux is larger and the conductive flux is smaller compared to the black ceiling. The radiative flux increases because the sample receives radiation from not only the flame but also the ceiling. The smaller the duct height, the greater the additional radiative flux the sample receives. This implies a higher sample surface temperature (confirmed in the numerical results), and hence a lower conductive flux compared to the results from the black ceiling. At large duct heights, conductive transfer still dominates in the pyrolysis process for the reflecting ceiling. At small duct heights, radiative and conductive heat input become comparable.

The total net heat inputs in the pyrolysis and preheat regions are compared in Fig. 11. The net heat input is the conductive and radiative heat from the flame and from the ceiling minus radiative heat loss from the sample surface. Compared to the black ceiling, the additional radiation feedback from the reflecting ceiling in general increases the net heat input to the solid. In the pyrolysis region, the increase of the net heat input is largest in the middle

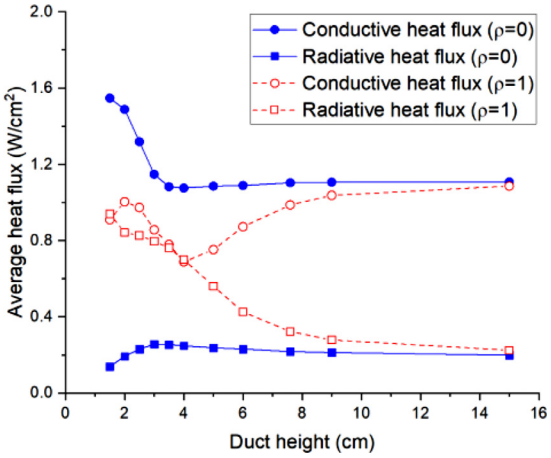

Fig. 10. Average heat flux in the pyrolysis zone on the sample surface.

duct height (Fig. 11a). As mentioned earlier, although ceiling reflection increases the radiative heat input on the sample surface, it also increases the surface temperature and decreases the conductive flux. The higher sample surface temperature also results in a higher surface radiation heat loss. As the duct height decreases, this effect becomes more prominent and eventually leads to similar net heat input to the pyrolysis region for black and reflecting ceilings at small duct heights (< 2 cm). This contributes to the nearly constant pyrolysis length at small duct height when ρ varies (Fig. 5). In the preheat region, the effect of enhanced heating due to ceiling reflection remains even when the duct height approaches the quenching height (Fig. 11b). This explains the stronger dependency of the spread rate on the ceiling reflectance compared to the pyrolysis length at small duct heights shown in Fig. 5.

Conclusion

Numerical studies are performed using an in-house three-dimensional transient CFD code to investigate purely forced concurrent-flow flame spread over a thin solid in a flow duct. The numerical model is shown to be able to capture the transient flame spread process and reproduce the effects of confinement on flame spread in the ISS microgravity experiments, Confined Combustion. The height of the flow duct and the reflectance of the duct wall are varied in the numerical investigation. Flame characteristics at the steady state between different cases are compared. The aerodynamics and thermal interactions between the flame and the duct wall are examined in detail. The key findings are as follows.

1) For any fixed wall reflectance, the flame spread rate and the pyrolysis length at steady state first increase and then decrease when the flow duct height decreases. Eventually, the flame fails to spread when the quenching duct height is reached. The flow confinement imposed by the duct has multiple effects on the flame spread process. Confinement accelerates the flow when the flow undergoes thermal expansion during combustion. Confinement also forces the flame to stay close to the sample surface, enhancing the net heat flux and local solid burning rate near the upstream flame base. These effects intensify the flame. However, at small duct heights, confinement limits the oxygen supply to the flame in the downstream region. The flame loses heat to the duct walls through conduction and radiation, reducing the flame strength. These competing effects result in the non-monotonic trend of the flame spread rate and pyrolysis length at different duct heights.
2) When the half duct height is reduced close to the flame height, the flame extends to the duct ceiling, blocking the downstream region from oxygen. The combustion efficiency decreases and the equivalence ratio increases with decreased duct height. At the optimal duct height, the equivalence ratio exceeds unity and the flame front transits from a center-leading convex shape to a side-leading concave shape. This side-leading concave flame front increases flammability in two ways. First, it increases the surface to volume ratio of the flame and facilitates the oxygen transport to the reaction zone from the two sides. Second, the flame length is extended further downstream to the pyrolysis region (i.e., flame-pyrolysis length ratio increases). This results in a larger preheat region and enhanced heat transfer to the solid.
3) At any fixed duct height, pyrolysis length and flame spread rate generally increase with the duct ceiling reflectance. This is because reflection from the ceiling increases the net heat input in both pyrolysis and preheat regions. For duct height smaller than the optimal duct height, the heat input enhancement is more pronounced in the preheat region than in the pyrolysis region. This is partly due to the increased flame-pyrolysis length ratio. As a result, at small duct heights, when ceiling reflectance increases, the flame spread rate increases but the pyrolysis length remains similar. The momentum loss to the duct ceiling also contributes to similar flame lengths at small duct heights when reflectance increases. In the gas phase, the combustion gas products (e.g., CO2 and H2O) also absorb the ceiling

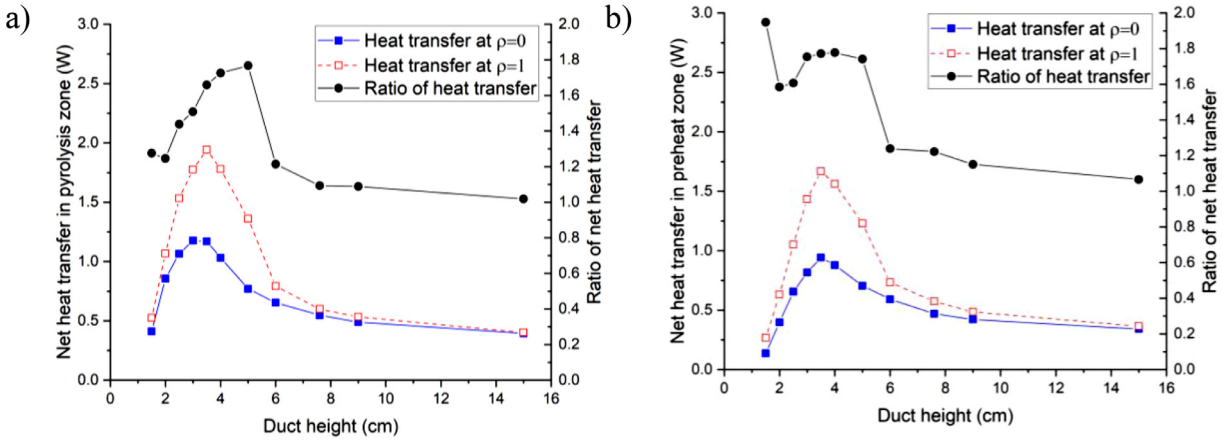

Fig. 11. Net heat input on the sample surface a) in the pyrolysis region and b) in the preheat region.

radiation, and hence the flame temperature increases as the reflectance increases.

4) The effect of the ceiling reflectance on the flame spread process is most prominent for middle duct heights. At large duct heights, the sample and the flame are far from the duct ceiling. The view factor from the flame to the adjacent ceiling area is small. At small duct heights, the combustion is limited by the oxygen supply (ventilation-controlled). In either case, gas phase combustion is correspondingly less sensitive to ceiling reflection.

Declaration of Competing Interest

None.

Acknowledgment

This research is co-sponsored by the National Science Foundation (NSF) and Center for the Advancement of Science in Space (CASIS) under grant number CBET-1740478.

The authors thank Dr. Paul Ferkul and Dr. Michael Johnston for their inputs on this work. We also thank the predecessors who contributed to the inhouse combustion code used in this work. We thank Xiaoyang Zhao for his tremendous effort on tuning modeling parameters and validating the model against previous microgravity experiments (BASS). Their efforts ensured the accuracy and validity of the numerical computations in this work.

We sincerely appreciate the tremendous support from CASIS, NASA Glenn Research Center, Marshall Spaceflight Center, ZIN Technologies (especially from Charles Bunnel, Emily Griffin, Steve Lawn, Russell Valentine, Beth Curtis, Chris Rogers, Wendell Booth), the Microgravity Science Glovebox team, and ISS crew members (Christina Koch, Jessica Meir, Andrew Morgan, Luca Parmitano, Shannon Walker, and Michael Hopkins). Their support on the ISS experiments makes this numerical study possible.

This numerical study made use of the High Performance Computing Resource in the Core Facility for Advanced Research Computing at Case Western Reserve University.

References

[1] M. Ahrens, B. Evarts, Fire Loss in the United States During 2019, National Fire Protection Association, Quincy, MA, USA, 2020.
[2] London Fire BrigadeLondon Fire Brigade Operational Response to Grenfell Tower, London Fire Brigade, London, UK, 2018.
[3] B.Y. Lattimer, U. Sorathia, Thermal characteristics of fires in a noncombustible corner, Fire Saf. J. 38 (2003) 709–745.
[4] M. Poreh, G. Garrad, A study of wall and corner fire plumes, Fire Saf. J. 34 (2000) 81–98.
[5] K.L. Jamison, D.A. Boardman, A new fire performance test for cavity wall insulation, MATEC Web Conf. (2016) 02004 paper.
[6] L.H. Hu, W. Peng, R. Huo, Critical wind velocity for arresting upwind gas and smoke dispersion induced by near-wall fire in a road tunnel, J. Hazard. Mater. 150 (2008) 68–75.
[7] X. Tian, M. Zhong, C. Shi, P. Zhang, C. Liu, Full-scale tunnel fire experimental study of fire-induced smoke temperature profiles with methanol-gasoline blends, Appl. Therm. Eng. 116 (2017) 233–243.
[8] M.C. Johnston, J.S. T'ien, D.E. Muff, X. Zhao, S.L. Olson, P.V. Ferkul, Self induced buoyant blow off in upward flame spread on thin solid fuels, Fire Saf. J. 71 (2015) 279–286.
[9] G. Markstein, J.d. Ris, Upward fire spread over textiles, Symp. (Int.) Combust. 14 (1973) 1085–1097.
[10] Y. Nakamura, T. Kashiwagi, K.B. McGrattan, H.R. Baum, Enclosure effects on flame spread over solid fuels in microgravity, Combust. Flame 130 (2002) 307–321.
[11] S. Wang, J. Hu, Y. Xiao, T. Ren, F. Zhu, Opposed-flow flame spread over solid fuels in microgravity: the effect of confined spaces, Microgravity Sci. Technol. 27 (2015) 329–336.
[12] P.V. Ferkul, J.S. T'ien, A model of low-speed concurrent flow flame spread over a thin fuel, Combust. Sci. Technol. 99 (1994) 345–370.
[13] Y.-.T. Tseng, J.S. T'ien, Limiting length, steady spread, and non-growing flames in concurrent flow over solids, J. Heat Transf.-Trans. ASME 132 (2010) 091201 paper.
[14] S.L. Olson, P.V. Ferkul, Microgravity flammability of PMMA rods in concurrent flow, 9th us national combustion meeting (2015), paper 2D01.
[15] X. Zhao, Y.-T.T. Liao, M.C. Johnston, J.S. T'ien, P.V. Ferkul, S.L. Olson, Concurrent flame growth, spread, and quenching over composite fabric samples in low speed purely forced flow in microgravity, Proc. Combust. Inst. 36 (2017) 2971–2978.
[16] C. Li, Y.-.T. Liao, Effects of ambient conditions on concurrent-flow flame spread over a wide thin solid in microgravity, Proc. Combust. Inst. 38 (2021) 4775–4784.
[17] D.L. Urban, P. Ferkul, S. Olson, G. Ruff, J. Easton, J.S. T'ien, Y.-T.T. Liao, C. Li, C. Fernandez-Pello, J. Torero, G. Legros, C. Eigenbrod, N. Smirnov, O. Fujita, S. Rouvreau, B. Toth, G. Jomaas, Flame spread: effects of microgravity and scale, Combust. Flame 199 (2019) 168–182.
[18] H.-.Y. Shih, J.S. T'ien, Modeling wall influence on solid-fuel flame spread in a flow tunnel, 35th Aerospace Science Meeting & Exhibit (1997), p. 0236. paper.
[19] H.-.Y. Shih, Flame spread and interactions in an array of thin solids in low-speed concurrent flows, Combust. Theory Model. 13 (2009) 443–459.
[20] V. Malhotra, C. Kumar, A. Kumar, Opposed flow flame spread over an array of thin solid fuel sheets in a microgravity environment, Combust. Theory Model. 17 (2013) 835–857.
[21] Y. Li, Y.-T.T. Liao, P. Ferkul, Numerical study of the effects of confinement on concurrent-flow flame spread in microgravity, J. Heat Transf.-Trans. ASME 142 (2020) 11301 paper.
[22] Y. Li, Y. Liao, P. Ferkul, Concurrent-flow flame spread over a thin solid in a narrow confined space in microgravity, Int. Mech. Eng. Congress Exposit. (2019) 11908 paper.
[23] Y. Li, Y.-T.T. Liao, P.V. Ferkul, M.C. Johnston, C. Bunnell, Experimental study of concurrent-flow flame spread over thin solids in confined space in microgravity, Combust. Flame 227 (2021) 39–51.
[24] Y.-T.T. Liao, J.S. T'ien, A numerical simulation of transient ignition and ignition limit of a composite solid by a localized radiant source, Combust. Theory Model. 17 (2013) 1096–1124.
[25] C. Li, Material Flammability and Burning Behavior of Thin Solids in Concurrent Forced Flow in Microgravity: A Numerical Study in Support of Large Scale Microgravity Burning Experiments, Case Western Reserve University: PhD Dissertation, Cleveland, OH, USA, 2020.
[26] A.C.Fernandez-Pello, Flame spread in a forward forced flow, Combust. Flame 36 (1979) 63–78.
[27] G.D. Grayson, K.R. Sacksteder, P.V. Ferkul, J.S. T'ien, Flame spreading over a thin solid in low-speed concurrent flow- Drop tower experimental results and comparison with theory, Microgravity Sci. Technol. 7 (1994) 187–195.
[28] A. Vetturini, W. Cui, Y.-T.T. Liao, S. Olson, P. Ferkul, Flame spread over ultra--thin solids: effect of area density and concurrent-opposed spread reversal phenomenon, Fire Technol 56 (2020) 91–111.
[29] A. Carney, Y. Li, Y.-.T. Liao, S. Olson, P.V. Ferkul, Concurrent-flow flame spread over thin discrete fuels in microgravity, Combust. Flame 226 (2021) 211–221 2021.
[30] S.L. Olson, F.J. Miller, S. Jahangirian, I.S. Wichman, Flame spread over thin fuels in actual and simulated microgravity conditions, Combust. Flame 156 (2009) 1214–1226.
[31] S.L. Olson, F.J. Miller, I.S. Wichman, Characterizing fingering flamelets using the logistic model, Combust. Theory Model. 10 (2006) 323–347.
[32] F. Incropera, D. Dewitt, T. Bergman, A. Lavine, Fundamentals of Heat and Mass Transfer - 6th Edition, John Wiley & Sons, Inc, Hoboken, NJ, USA, 2007.